Table 1 Heat of combustion and ignition properties of metals with ClF_3 and ClF_5

Metal, state, supplier	Heat of combustion, kcal/g	Performance with ClF_3		Heat of combustion, kcal/g	Performance with ClF_5	
		Hypergolic with gaseous ClF_3	Hypergolic with liquid ClF_3		Hypergolic with gaseous ClF_5	Hypergolic with liquid ClF_5
Li, 100 μm size, Foote Mineral Co.	4.156	X	X (2)[a]	4.469	X	X (1)
Be, 325 mesh powder, Brush Beryllium Co.	3.493			3.835		
Mg, 325 mesh powder, Reade Mfg. Co., Inc.	3.083		X (5)	3.320		
Ca, 325 mesh powder, Research Chemicals Div. of Nuclear Corp. of America	2.859	X	X (4)[b]	3.035	X	X (3)[b]
Al, 325 mesh powder, Reynolds Aluminum Co.	2.565	X	X	2.786		
Na, 0.0625-in.-diam wire, City Chemical Co.	2.544	[c]	[c]	2.676	X	X (6)
44 NaK,[d] liquid, MSA Research Inc.	2.293	[c]	X (8)	2.400	X	X (7)
56 NaK, liquid, MSA Research Inc.	2.216	X	X (10)	2.316	X	X (9)
78 NaK, liquid, MSA Research Inc.	2.062	[c]	X (12)	2.149	X	X (11)
K, Small chunks, J. T. Baker Chemical Co.	1.891	X	X (14)	1.963	X	X (13)

[a] Numbers in parentheses indicate the recommended fuel/oxidizer combinations in order of declining preference.
[b] Selected because this reactant combination was extremely hypergolic.
[c] An oxide coating may have prevented ignition.
[d] An alloy of Na and K, containing 44% K by weight.

of the components may fail. Consequently, a heat source should be provided for the spacecraft to protect these components. The heat source may be based on nuclear reactors (or isotope disintegration) or chemical phase changes, or chemical reactions.

Systems analyses have indicated that when the unmanned spacecraft lander is designed to operate on the Martian surface for durations of several terrestrial days or less, then the optimum source of heat is a chemical reaction.[1] The selection of reactants for a chemical spacecraft heater is subject to the following requirements: 1) the reaction should produce the highest possible combustion energy per unit mass of the reactants, 2) the reactants must be hypergolic, 3) the reaction products should be solid, to avoid venting problems, and 4) the reactants should be heat-sterilizable.

The purpose of this Note is to propose reactant combinations that conform to the foregoing requirements. The oxidizers selected were ClF_3 and ClF_5, and the fuels were various metals. Table 1 presents the metals selected, the computed heats of combustion per unit mass of reactants (metal and liquid oxidizer in stoichiometric proportions), and experimental findings as to whether these metals ignited on contact with either gaseous or liquid ClF_3 or ClF_5 at ambient temperatures and pressure.

Experimental Procedure

To determine whether the metals ignited in gaseous or liquid ClF_3 or ClF_5, a stream of the oxidizer was directed at the metal (0.1–0.9 g), contained in a size 000000 Coors crucible. The experiments were performed in the open; the gaseous oxidizer was directed through a $\frac{1}{8}$-in. tubing, with the tip approximately $\frac{1}{2}$ in. above the crucible. The liquid ClF_3(ClF_3 was obtained from the Matheson Company and used without further purification) was also directed through the $\frac{1}{8}$-in. line, whereas the liquid ClF_5(ClF_5 was obtained from the Allied Chemical Company and used without further purification) was first condensed into a cooled test tube and then carefully poured onto the metal.

The Na, K, and NaK alloys reacted very quickly with air, forming protective oxide coatings prior to exposure to the oxidizers. Nevertheless, these substances inflamed upon contact with the gaseous oxidizers, as will be shown in the following section.

The computations for the heat of combustion per unit mass of reactants were based on thermodynamic data.[2] The ΔH_f of ClF_5 is not available in the literature, but its value was assumed to be −60 kcal/mole.

Results and Discussion

In considering the results (Table 1) on the basis of the design criteria, it is seen that all of the reactants are heat sterilizable. Nearly all of the reactant combinations are hypergolic. Therefore, the recommended fuel oxidizer combinations, in order of declining preference, are indicated by the numbers in parentheses in Table 1, number 1 being best. Thus, the preferred fuel to be used with either ClF_3 and ClF_5 as the oxidizer for a chemical spacecraft heater would be either Li or Ca. A prototype of a spacecraft chemical heater should be built, and the performance of the proposed reactants should be determined in test runs.

References

[1] Young, D. L. and Dipprey, D. F., "The Utilization of Planetary Atmospheres for Power and Propulsion Operations," presented at the Fifth Annual Meeting of the Working Group on Extraterrestrial Resources, Marshall Space Flight Center, Huntsville, Ala., March 1–3, 1967.

[2] *Selected values of chemical thermodynamic properties*, Circular 500, National Bureau of Standards, Washington, D. C., 1952.

Approximate Analysis of Nonisentropic Flow in Conical Nozzles

JOE D. HOFFMAN*
Purdue University, Lafayette, Ind.

Nomenclature

a = speed of sound, $(\gamma Rt)^{1/2}$
A_p, A_s = planar and spherical exit areas, respectively
A_t = geometric throat area, πy_t^2
A_* = minimum flow area (effective throat area)
b = $(n-1)/(\gamma-1)$

Received July 11, 1969; revision received August 25, 1969.
* Associate Professor of Mechanical Engineering. Member AIAA.

c_p = specific heat at constant pressure
C_c = geometric contraction factor, A_*/A_t
C_F = thrust coefficient, F/P_cA_t
C_{F^o} = thrust coefficient for parallel, uniform flow
C_η = nonisentropic mass flow efficiency factor
F = thrust
h,H_c = enthalpy and chamber stagnation enthalpy, respectively
I_{sp} = specific impulse, $F/\dot{m}$
L^* = nondimensional nozzle length, L/y_t
$\dot{m}$ = mass flow rate, ρAV (actual, nonisentropic)
M = Mach number, V/a
n = polytropic exponent, $p\rho^{-n}$ = const
p,p_o = pressure and ambient pressure, respectively
P_c = chamber stagnation pressure
Q = parameter defined by Eq. (23)
r,r_o = p/P_c and p_o/P_c, respectively
R = gas constant
R^* = nondimensional source flow radius, R_s/y_t
t,T_c = temperature and chamber stagnation temperature, respectively
V = velocity
y_t = throat radius
Y = parameter defined by Eq. (22)
α = cone half-angle
γ = specific heat ratio
Γ = $[2/(\gamma+1)]^{(\gamma+1)/2(\gamma-1)}$
ϵ = geometric area ratio, A_p/A_t
ϵ_g = gasdynamic expansion ratio, A_s/A^*
ϵ_s = geometric area ratio, A_s/A_t
η = kinetic energy efficiency, Eq. (2)
λ = divergence factor, $(1+\cos\alpha)/2$
ξ = $2/(\gamma+1)$
ρ = density
ρ_t^* = nondimensional throat radius of curvature, ρ_t/y_t
ψ $\equiv$ $[1+(\gamma-1)M^2/2]$

Subscripts

c = chamber stagnation condition
OPT = optimization condition
p,s = evaluated at A_p and A_s, respectively
$t,*$ = evaluated at A_t and A_*, respectively

Superscripts

$(\ )'$ = isentropic condition

Introduction

PERFORMANCE estimates for conical nozzles are commonly based on simple one-dimensional, isentropic flow theory and are corrected for three-dimensional, nonisentropic effects by the use of various coefficients; constant values for γ and R usually are assumed. At the other extreme are elaborate method of characteristics calculations that include nonequilibrium reacting flows, boundary-layer effects, etc. Various intermediate approximation techniques have been proposed. Durham[1] included a velocity coefficient and predicted a decrease in mass flow rate and thrust for nonisentropic flow, a trend that was substantiated by experimental results. Rowe[2] accounted for nonisentropic expansion beyond the throat by changing the expansion exponent discontinuously from γ to a polytropic exponent n at the throat. He considered three-dimensional-throat-flow and exit-divergence effects, but it appears that he used the divergence factor incorrectly. He developed an equation for the optimum operating condition, which predicted underexpansion of the flow (as does the present analysis), but he kept the cone half-angle α fixed, precluding optimization with respect to length. One of his numerical examples predicted a thrust maximu at an area ratio larger than that for isentropic flow at the same operating conditions, a result in direct contradiction with the results of Durham[1] (and the present analysis). Scofield and Hoffman[3] presented an analysis for determining the cone half-angle for maximum thrust of a conical nozzle of fixed length or surface area, neglecting three-dimensional-throat-flow and nonisentropic-flow effects but including the exhaust divergence factor $\lambda = (1+\cos\alpha)/2$.[4,5] Rao[6] discussed the three-dimensional flow-contraction effect in the throat region, and suggested the use of a flow coefficient to account for it.

The present analysis is based on one-dimensional, steady, adiabatic, source flow of a thermally and calorically perfect gas in a conical nozzle, but it accounts for nonuniform flow effects in the throat region (by a contraction factor[6] C_c), exit divergence effects (by λ), and nonisentropic flow effects (by a kinetic energy efficiency η). A parametric study illustrates each of these effects and provides insight into the coupling between C_c, η, λ, γ, and the ambient pressure p_o. Explicit boundary-layer effects are neglected.

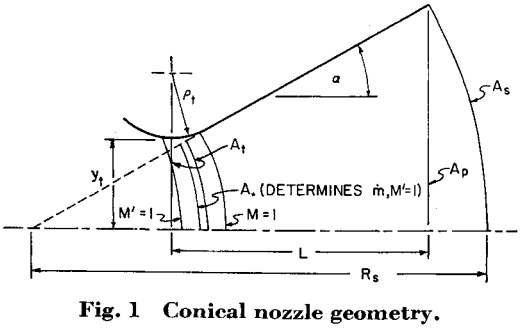

Fig. 1 Conical nozzle geometry.

Analysis

Properties are assumed to be constant on spherical flow surfaces A_s defined by the source flow radius R_s (Fig. 1). The geometric area ratio is $\epsilon = A_p/A_t$, and the gasdynamic expansion ratio is $\epsilon_g = A_s/A_*$, where A_* is the minimum flow area, which is related to A_t by the contraction factor $C_c = A_*/A_t \leq 1$. This C_c is assumed to be due entirely to three-dimensional flow effects in the throat region and can be evaluated independently of the actual flowfield. Thus, C_c can be determined by evaluating the isentropic, three-dimensional mass flow rate through A_t by any scheme whatsoever (e.g., Sauer's[7] or Hall's technique[8]), and then evaluating the equivalent isentropic one-dimensional A_* which would result in the same $\dot{m}$. The actual sonic line where $M' = 1$ and the equivalent-source-flow A_* are illustrated in Fig. 1. Also shown are the planar A_t and its equivalent in the source flowfield. In a nonisentropic flow, the minimum flow area will still be A_*, even though $M < 1$ there. The exit areas are related by $A_p = \lambda A_s$. In the following analysis, all gasdynamic properties are evaluated in terms of ϵ_g and the results are expressed in terms of ϵ, where $\epsilon = \lambda C_c \epsilon_g$.

The thermodynamic models are illustrated in Fig. 2. The reference isentropic and the actual nonisentropic expansion processes take place between P_c and the same static pressure p. Since expansion is assumed to be adiabatic,

$$H_c = h' + V'^2/2 = h + V^2/2 = \text{const} \qquad (1)$$

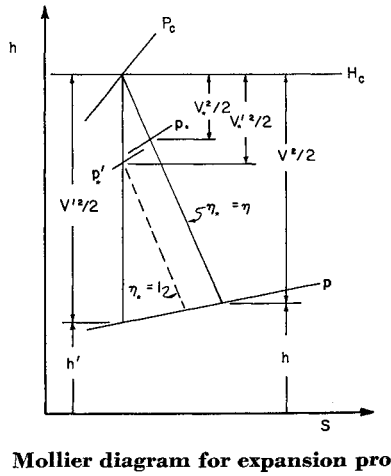

Fig. 2 Mollier diagram for expansion processes.

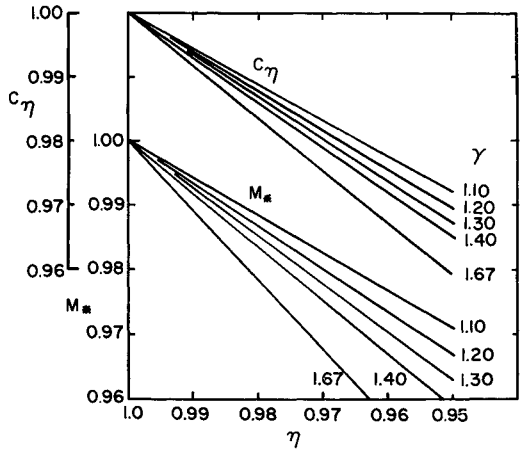

Fig. 3 Mass flow efficiency factor and minimum area Mach number.

Two possible nonisentropic expansion processes are shown. In the first, which is nonisentropic throughout ($\eta_* = \eta$), the nonisentropic (V) and isentropic (V') flow velocities are related by the kinetic energy efficiency,

$$\eta \equiv \frac{V^2/2}{V'^2/2} = \frac{H_c - h}{H_c - h'} = \frac{V^2/2}{c_p(T_c - t')} \tag{2}$$

In the second, the flow is assumed to be isentropic to $A_*(\eta_* = 1)$, and nonisentropic thereafter; a brief summary of results for this second scheme is given later. Values of η can be estimated by past experience with similar systems and generally lie in the range 0.95–1.0. Employing $a^2 = \gamma Rt$ and the relationship between c_p, γ, and R, we find

$$c_pT_c = a_c^2/(\gamma - 1) = a^2\psi/(\gamma - 1) \tag{3}$$

where $\psi \equiv 1 + (\gamma - 1)M^2/2 = T_c/t$, and $M = V/(\gamma Rt)^{1/2}$, i.e., in terms of nonisentropic flow properties. Substituting Eq. (3) into (2) and expressing the isentropic temperature ratio t'/T_c in terms of the actual pressure ratio $r \equiv p/p_c$, $t'/T_c = r^{(\gamma-1)/\gamma}$ yields

$$r = [1 - (\gamma - 1)M^2/2\eta\psi]^{\gamma/(\gamma-1)} \tag{4}$$

By continuity,

$$\dot{m}/A = pV/Rt = P_crM(\gamma\psi/RT_c)^{1/2} \tag{5}$$

Finding $d(\dot{m}/A)/dM$ from Eq. (5) and setting it equal to zero yields a simple quadratic equation for the minimum area Mach number,

$$M_*^4(\eta - 1) + M_*^2[3\eta - (3\gamma - 1)/(\gamma - 1)] \times (\gamma - 1)^{-1} + 2\eta(\gamma - 1)^{-2} = 0 \tag{6}$$

which can be solved numerically. The results (Fig. 3) are correlated by the empirical expression

$$M_* = 1 - (1 - \eta)[0.5 + 0.9(\gamma - 1)] \tag{7}$$

The effect of the nonisentropic process on $\dot{m}$ can be expressed in terms of a mass flow efficiency factor, $C_\eta = \dot{m}_{\eta<1}/\dot{m}_{\eta=1}$, where the isentropic mass flow rate is given by $\dot{m}_{\eta=1} = \Gamma P_cA_*(\gamma/RT_c)^{1/2}$. Equation (5) for $\dot{m}_\eta$ can also be evaluated at A_*, and the result yields

$$C_\eta = M_*r_*\psi_*^{1/2}/\Gamma \tag{8}$$

All terms in Eq. (8) are functions of M_*, which can be evaluated by Eq. (6). Thus, C_η is a function only of γ and η. The C_η results (Fig. 3) are correlated by the empirical equation

$$C_\eta = 1 - (1 - \eta)\gamma/2 \tag{9}$$

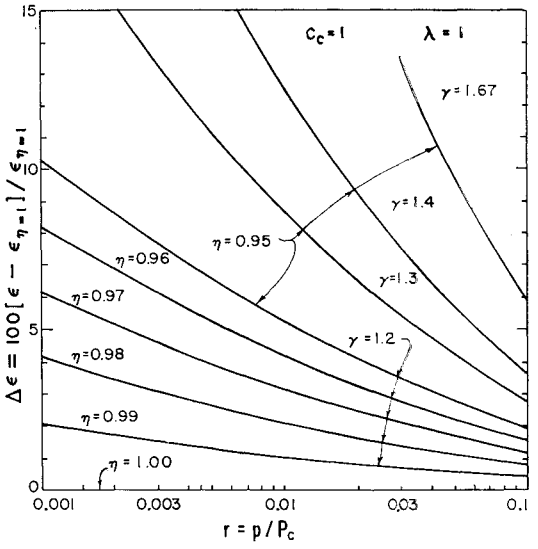

Fig. 4 Area ratio for nonisentropic expansion.

The product of C_c and C_η is the conventional throat discharge coefficient $C_D = C_cC_\eta$. (A third factor, not considered explicitly in this analysis, is the boundary-layer displacement thickness, which also reduces A_*. If required, this effect can be accounted for in C_c.) The geometric area ratio ϵ can be related to the flow properties by evaluating Eq. (5) at A_* and at A_s and employing $\epsilon = \lambda C_c\epsilon_g$. Thus,

$$\epsilon = A_p/A_t = \lambda C_cC_\eta\Gamma/Mr\psi^{1/2} \tag{10}$$

All terms in Eq. (10) can be evaluated in terms of M (or r) yielding an explicit relationship between ϵ and r, with γ and η as parameters. Numerical results are presented in Fig. 4 for various η's with $\gamma = 1.2$, and various γ's with $\eta = 0.95$, assuming $C_c = 1$ and $\lambda = 1$. ($C_c < 1$ or $\lambda < 1$ reduces ϵ in direct proportion.) The results are presented in terms of $\Delta\epsilon$, the percentage change in ϵ from the ϵ required for isentropic expansion to the given pressure ratio r. This $\Delta\epsilon$ is always positive; i.e., nonisentropic flows require larger ϵ's than do isentropic flows to attain a given r.

The thrust coefficient C_F is given by

$$C_F = F/P_cA_t = \lambda[(\dot{m}V/P_cA_t) + (r - r_o)C_c\epsilon_g] = \lambda C_{F^o} \tag{11}$$

wherein we can substitute

$$\dot{m}V/P_cA_t = C_cC_\eta\gamma\Gamma(V/a_c) \tag{12}$$

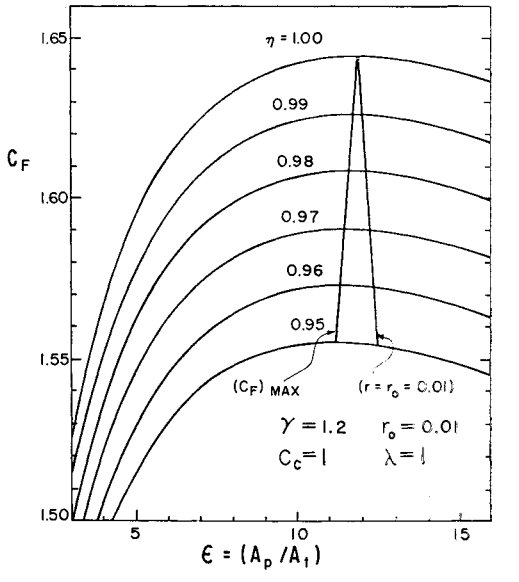

Fig. 5 Thrust coefficient for nonisentropic expansion.

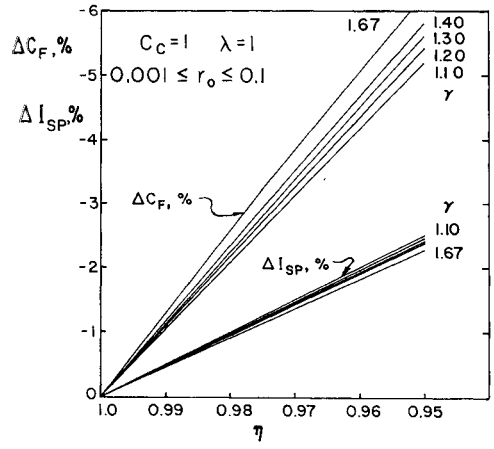

Fig. 6 Effects of η and γ on performance.

Here V and p are evaluated on the spherical flow area A_s, $r_o = p_o/P_c$, and $C_F{}^o$ is the thrust coefficient for parallel, uniform flow. Expressions have been developed for evaluating $\dot{m}$, λ, r, and ϵ_g in terms of ϵ. Combining Eq. (2) and $t'/T_c = r^{(\gamma-1)/\gamma}$ yields

$$V/a_c = \{2\eta(\gamma - 1)^{-1}[1 - r^{(\gamma-1)/\gamma}]\}^{1/2} \quad (13)$$

Substitution of (13) into (12) and into (11) yields the working equation for C_F;

$$C_F = \lambda\{C_c C_\eta \gamma\Gamma[2\eta(\gamma - 1)^{-1}(1 - r^{(\gamma-1)/\gamma})]^{1/2} + C_c(r - r_o)\epsilon_g\} \quad (14)$$

Figure 5 shows that C_F exhibits the usual trend with respect to ϵ for a fixed ambient pressure. A decrease in η results in an almost proportionate decrease in C_F (e.g., $\eta = 0.95$ yields a 5.4% decrease in C_F at $\epsilon = 11.87$). The ϵ for "adapted" ($p = p_o$) nozzle performance increases as η decreases, but the ϵ for maximum performance ($C_{F_{OPT}}$) decreases as η decreases. This effect was also noted by Durham.[1] Thus, two conclusions are 1) nonisentropic flow results in a significant decrease in C_F, and 2) the ϵ for $C_{F_{OPT}}$ decreases as η increases and differs significantly from the ϵ required for complete expansion.

The specific impulse for nonisentropic flow is

$$I_{sp} = F/\dot{m} = C_F(a_c/C_c C_\eta \gamma\Gamma) \quad (15)$$

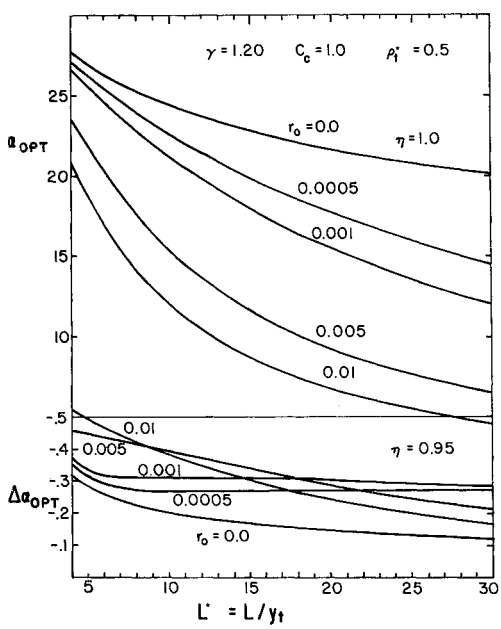

Fig. 7 Design chart for variable cone angle.

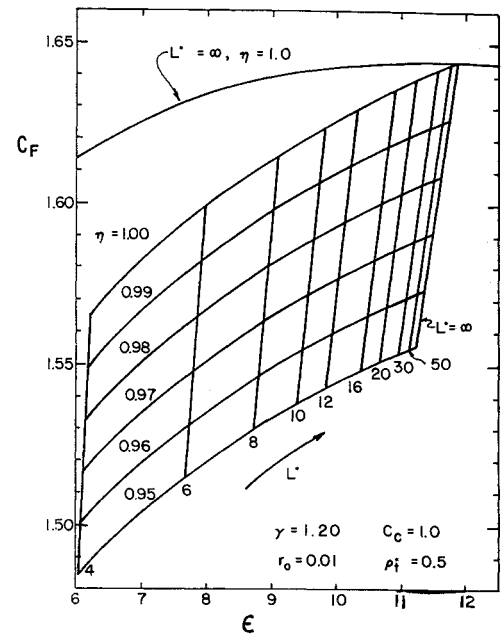

Fig. 8 Effects of η and α on performance.

For fixed chamber conditions (i.e., a_c, γ, and Γ), $I_{sp} \propto C_F/C_c C_\eta$. Also, C_F decreases when C_c or C_η decreases as specified by Eq. (14). However, the effects of C_c and C_η on I_{sp} are smaller than on C_F. This occurs because $C_F \propto F$, which depends on both $\dot{m}$ and the expansion properties p and V. Since $\dot{m}$ is decreased by the nonisentropic effects, F decreases due to both effects. However, I_{sp} does not depend directly on $\dot{m}$, but basically only on the expansion properties p and V. Hence, I_{sp} is a better measure of the performance loss than C_F.

Optimization

We can relate α and λ to the nozzle geometry, and thus to r, by the following equations[3]:

$$\epsilon_s \equiv A_s/A_t = 2R^{*2}(1 - \cos\alpha) \quad (16)$$

$$R^* = L^* \sec\alpha + \csc\alpha[1 + \rho_t^*(1 - \sec\alpha)] \quad (17)$$

where R^*, L^*, and ρ_t^* are the source flow radius, nozzle length, and throat radius of curvature nondimensionalized by the throat radius y_t. Thus, Eq. (11) implicitly relates C_F to r. The condition for a maximum is

$$dC_F/dr = C_F{}^o(d\lambda/dr) + \lambda(dC_F{}^o/dr) = 0 \quad (18)$$

From the definition of λ,

$$d\lambda/dr = -\sin\alpha(d\epsilon_s/dr)/2(d\epsilon_s/d\alpha) \quad (19)$$

where $d\epsilon_s/d\alpha$ is obtained from Eqs. (16) and (17);

$$d\epsilon_s/d\alpha = 2R^*\{R^* \sin\alpha + 2(1 - \cos\alpha)[L^* \tan\alpha \sec\alpha - (1 + \rho_t^*)\cot\alpha \csc\alpha - \rho_t^* \csc^2\alpha(\tan^2\alpha - 1)]\} \quad (20)$$

From Eqs. (4) and (10),

$$d\epsilon_s/dr = -\epsilon_s/\gamma r Y M^2 \quad (21)$$

where

$$Y = \{\gamma M^2 - Q[1 + (\gamma - 1)M^2]\}^{-1} \quad (22)$$

and

$$Q = \eta - (\gamma - 1)M^2(1 - \eta)/2 \quad (23)$$

From Eq. (14), $dC_F{}^o/dr$ is given by

$$dC_F{}^o/dr = -\epsilon_s Q + (r - r_o)d\epsilon_s/dr + \epsilon_s \quad (24)$$

Substituting Eqs. (19, 21, and 24) into Eq. (18) yields the following optimization condition:

$$(r - r_o)_{OPT} = \frac{C_{F^o} \sin\alpha}{(1 + \cos\alpha)(d\epsilon_s/d\alpha)} + (1 - Q)\gamma r Y M^2 \quad (25)$$

The first term on the right is the design condition obtained in Ref. 3 for isentropic flow. For a fixed α, this term vanishes; when present, it is always positive. The second term arises from the nonisentropic flow effects and also is always positive. When the flow is isentropic, $\eta = 1$, and Eq. (23) reduces to $Q = 1$, so this second term vanishes. Thus, both effects, variable α and nonisentropic flow, require underexpansion of the flow to obtain maximum performance. Iterative techniques were employed to solve Eq. (25) for r in terms of r_o, γ, C_c, and α.

Results for fixed cone angle **($\lambda = 1$)**

Solutions for $\lambda = 1$ and various η's show the rather large amount of underexpansion required to obtain maximum thrust; e.g., $p \simeq 1.15\ p_o$ when $p_o/P_c = 0.01$ and $\eta = 0.95$. Results not shown for r_o up to 0.1 and γ's ranging from 1.1 to 1.4 are well correlated by

$$(r - r_o)_{OPT} = (0.015 + 5.8r_o)(1 - \eta)(\gamma - 0.8) \quad (26)$$

The resulting $\Delta\epsilon_{OPT}$ (%) due to nonisentropic effects is almost proportionate to the decrease in η and is insensitive to r_o for a given η; it is well correlated by

$$\Delta\epsilon = 1.1(1 - \eta)[1 - 0.7(\gamma - 1.4)^2] \quad (27)$$

Figure 6 presents the losses in C_F and I_{sp} (as percentages of their isentropic values) at optimum expansion ratios for $C_c = 1$, $\lambda = 1$, r_o between 0.001 and 0.1, and γ from 1.1 to 1.67. The losses in I_{sp} are $\cong$46% as large as the C_F losses. The effect of γ is small in comparison with the effect of η. Because of the flat nature of the C_F curves near their maximums in Fig. 5, the foregoing results are quite good for evaluating performance losses for a wide range of ϵ's ($8 < \epsilon < 15$). The results in Fig. 6 are well correlated by

$$\Delta C_F = -(1 - \eta)[1 + 0.4(\gamma - 1)] \quad (28)$$

$$\Delta I_{sp} = -(1 - \eta)[0.5 - 0.1(\gamma - 1.1)] \quad (29)$$

Results for variable α and η

Equation (25) was employed, along with Eqs. (16, 17, and 20), to obtain α_{OPT} vs L^* for maximum performance. The top part of Fig. 7 gives typical curves for $\eta = 1$ (as was predicted in Ref. 3), whereas the bottom part shows the changes ($\Delta\alpha_{OPT}$) caused by decreasing η from 1.0 to 0.95. A curve for vacuum expansion ($r_o = 0$) is included. In all cases, $\Delta\alpha_{OPT}$ is negative; i.e., the ϵ for maximum performance is smaller when $\eta < 1$.

Figure 8 illustrates the effect on performance of variable α for $\gamma = 1.2$, $r_o = 0.01$, $C_c = 1.0$, $\rho_t{}^* = 0.5$, and η ranging from 0.95 to 1.0. The effect of L^* is clearly illustrated. The curve across the top ($L^* = \infty$, $\eta = 1$) is the same as presented in Fig. 5.

The effect of throat radius of curvature, $\rho_t{}^* = \rho_t/y_t$, was investigated by varying it from 0 to 2. At each L^*, ϵ and hence C_F were slightly reduced as $\rho_t{}^*$ was increased, but the magnitudes of the effects were generally insignificant, amounting to 0.2% in C_F at the extreme condition of $L^* = 4$ and $\rho_t{}^* = 2$.

The effects of off-design performance for nozzles optimized for $\eta = 1$ when operated at $\eta < 1$ were investigated as follows: λ and r were obtained, for given L^* and ϵ, from the equations developed herein, and C_F for the off-design condition was evaluated from Eq. (14). The loss in C_F is $\cong$ 1% for each 0.01 step decrease in n. The loss is almost independent of L^* but is slightly smaller at very short lengths.

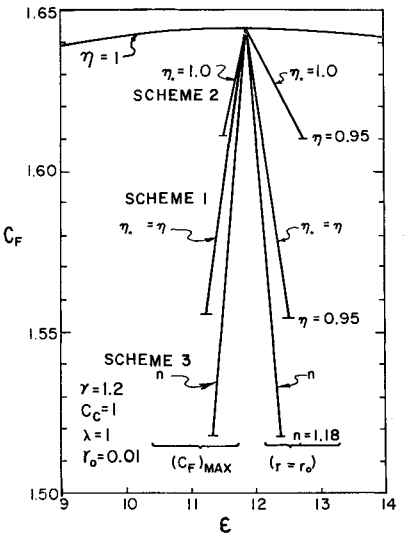

Fig. 9 Comparison of nonisentropic flow models.

Other Nonisentropic Processes

Two other techniques for specifying the nonisentropic effects were investigated. Scheme 2 (illustrated in Fig. 2) uses a kinetic energy efficiency η, but assumes that $\eta = 1$ up to the minimum flow area A_*, so that $C_\eta = M_* = 1.0$. The ϵ is still given by Eq. (10), where M and r are now related by

$$r = \{\xi[1 - (\gamma - 1)(M^2 - 1)/2\eta\psi]\}^{\gamma/(\gamma-1)} \quad (30)$$

and

$$V/a_c = \xi^{1/2}\{1 + 2\eta[1 - \xi^{-1}r^{(\gamma-1)/\gamma}]\}^{1/2} \quad (31)$$

Now C_F is found by substituting Eq. (31) into (12) into (11). The I_{sp} is still given by Eq. (15). The optimization condition is now given by Eq. (25) when the parameter Q in Eqs. (22) and (25) is replaced by $\xi[Q + (\gamma - 1)/2]$.

Scheme 3 uses a polytropic exponent n, which is constant during the entire expansion process. (Rowe[1] used a polytropic exponent but assumed isentropic flow to the throat.) For Scheme 3,

$$(p/P_c)^{(n-1)/n} = (\rho/\rho_c)^{n-1} = (t/T_c) = \psi^{-1} \quad (32)$$

and

$$V/a_c = \{2(\gamma - 1)^{-1}[1 - r^{(n-1)/n}]\}^{1/2} \quad (33)$$

The minimum-area Mach number is $M_* = [(n - 1)/(\gamma - 1)]^{1/2} \equiv b^{1/2}$. The C_η and ϵ are still given by Eqs. (8) and (10) wherein M and r are now related by Eq. (32), and C_F is found by substituting Eq. (33) into (12) and into (11). The I_{sp} is still given by Eq. (15). The optimization condition is

$$(r - r_o)_{OPT} = C_{F^o} \sin\alpha/(1 + \cos\alpha)(d\epsilon_s/d\alpha) + M^2(n - \gamma b)[(M^2 - b)\psi^{n/(n-1)}]^{-1} \quad (34)$$

where the first term due to α effects is the same as for the other two schemes.

The three schemes are compared for $\gamma = 1.2$, $C_c = 1.0$, $r_o = 0.01$, and $\lambda = 1$ in Fig. 9, which presents loci of $(C_F)_{MAX}$ and $(r - r_o)$ expansions. The isentropic performance curve crossing the top of Fig. 9 and the $\eta_* = \eta$ results are the same as shown in Fig. 5. The results for $\eta_* = 1.0$ are identical in trend to those for $\eta_* = \eta$, and the performance losses are not as great. The results based on the polytropic exponent n are also identical in trend to the results based on η. Results such as presented in Figs. 3–8 were obtained for the other two nonisentropic flow models, and the trends were the same. Of course, for $\eta_* = 1.0$, the throat trends were different ($C_\eta = M_* = 1.0$), and the percentage losses in

I_{sp} and C_F were the same since $\dot{m}$ is unaffected by the nonisentropic effects. The identical trends exhibited by flow models 2 and 3 lend great support to the methods and results obtained in this study.

Conclusions

In any actual rocket motor, effects not included here are present which would tend to change the results somewhat. However, the trends illustrated by the results presented herein for an arbitrary nonisentropic process should be useful in gaining insight into the coupled effects of C_c, η, α, γ, and r_o on conical nozzle performance and design. The most significant conclusion reached in this study is that in real systems subject to nonisentropic flow effects, maximum performance always requires some finite amount of underexpansion and a correspondingly smaller area ratio than does isentropic expansion.

References

[1] Durham, F. P., "Thrust Characteristics of Underexpanded Nozzles," *Jet Propulsion*, Vol. 25, No. 12, Dec. 1955, pp. 696–700.

[2] Rowe, P. N., "The Thrust of a Supersonic Conical Nozzle with Non-Isentropic Flow," *Proceedings of the Institution of Mechanical Engineering*, Vol. 172, No. 30, 1958, pp. 877–888.

[3] Scofield, M. P. and Hoffman, J. D., "Optimization of Conical Thrust Nozzles," *Journal of Spacecraft and Rockets*, Vol. 4, No. 11, Nov. 1967, pp. 1547–1549.

[4] Landsbaum, E. M., "Thrust of a Conical Nozzle," *ARS Journal*, Vol. 29, No. 3, March 1959, pp. 212–213.

[5] Malina, F. J., "Characteristics of the Rocket Motor Unit Based on the Theory of Perfect Gases," *Journal of the Franklin Institute*, Vol. 230, 1940, pp. 433–454.

[6] Rao, G. V. R., "Evaluation of Conical Nozzle Thrust Coefficient," *ARS Journal*, Vol. 29, No. 8, Aug. 1959, pp. 606–607.

[7] Sauer, R., "General Characteristics of the Flow Through Nozzles at Near Critical Speeds," TM 1147, June 1947, NACA.

[8] Hall, I. M., "Transonic Flow in Two-Dimensional and Axially Symmetric Nozzles," *Quarterly Journal of Mechanics and Applied Mathematics*, Vol. XV, Pt. 4, 1962, pp. 487–508.

Ablative Materials for Controlled High Regression Rates in Rocket Motors

H. O. Davis* and H. M. Evensen†
Aerojet-General Corporation, Sacramento, Calif.

THE conventional method of obtaining a neutral pressure curve in a solid rocket motor involves special, and at times, complex grain designs. Tactical rocket motors operating at high pressures with high burning rate propellants are subjected to high-acceleration loads which impose structural limitations on propellant grain configurations. The simplest grain, from a structural point of view, is an internal burning cylinder that would produce a progressive pressure curve. By combining this with a nozzle throat area increase at a rate proportional to the mass flow rate increase caused by surface area increase, an essentially neutral pressure curve can be obtained. Thus, there is no further increase in r_b due to P_c change (which would compound the acceleration problem).

Regression rates can be varied by affecting changes in the individual ablative material. However, the regression required for the Zero Antiaircraft Potential (ZAP) motor‡ appeared to be beyond the scope of any variation in the standard ablatives such as carbon, silica, or asbestos reinforcement since a regression rate of approximately 0.30 in./sec was needed. It was unlikely that a standard material could be tailored to produce a regression rate of this magnitude. Furthermore, a low density or resin modification significant enough to achieve the desired increase would likely produce nonuniformities and erratic performance. The highest regression obtained for a standard carbon phenolic had been 0.018/sec for a similar pressure and environment as the ZAP motor. Two general categories of materials were considered: 1) single component: melt formers (e.g., aluminum) and sublimers (e.g., polytetrafluoroethylene); 2) composite materials.

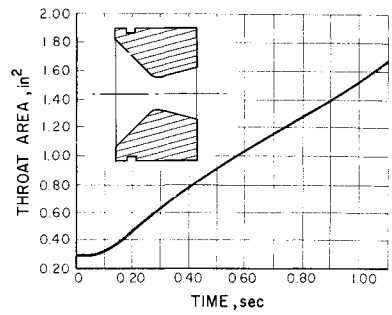

Fig. 1 Throat area-time function for ZAP nozzle material evaluation in 3KS-1000 motor (inset-test nozzle configuration).

Within the composite materials, three basic resin systems were considered: polyesters, epoxies, and phenolics. Reinforcements considered include a wide range of thermoplastic and thermosetting materials, entailing melt formers, sublimers, and char formers. The thermoplastics are primarily reduced to decomposition gases and leave very little residue. Thermosetting materials decompose, leaving various amounts of residue depending on the polymer structure.

From data in Ref. 1, it appeared that glass and nylon-reinforced phenolics would be candidates.

Compatibility with the propellant exhaust gases was considered to the extent that if oxidation was to be the controlling mechanism of material removal, a low char density would be required. The mechanical removal of a low-density char was also a method of achieving a high regression rate. A low melt temperature in conjunction with a low viscosity offered still another mechanism. These analyses had to be qualitative because of the lack of empirical data and the lack of comparative test conditions. Availability and cost were also important, of course.

Subscale Screening Tests

A subscale motor identified as 3KS-1000, used primarily for propellant evaluation, was selected as the test vehicle for evaluating the candidate materials. The throat insert configuration is shown in Fig. 1. The motor was designed to have an average chamber pressure ($\bar{P}_c$) of about 2000 psi.

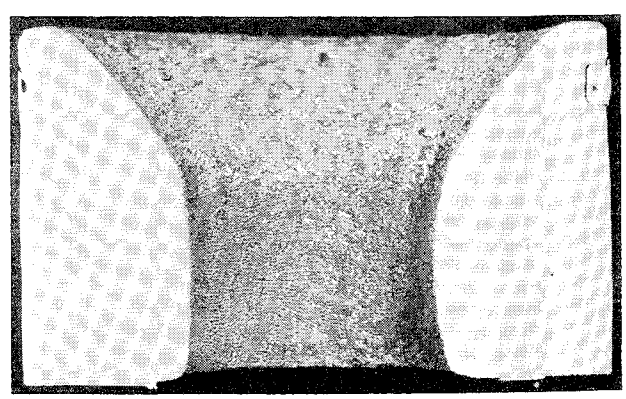

Fig. 2 Postfire photograph of a cross section from nylon/phenolic with 50% resin content.

Presented as Paper 69-423 at the AIAA 5th Propulsion Joint Specialist Conference, U.S. Air Force Academy, Colo., June 9–13, 1969; submitted June 16, 1969; revision received August 18, 1969.

* Engineering Specialist.

† Supervisor. Member AIAA.

‡ Developed under Contract N60921-68-C-0225.